Journal of Magnetic Resonance 204 (2010) 281–289

Contents lists available at ScienceDirect

Journal of Magnetic Resonance

journal homepage: www.elsevier.com/locate/jmr

Magnetic field modeling with a set of individual localized coils

Christoph Juchem *, Terence W. Nixon, Scott McIntyre, Douglas L. Rothman, Robin A. de Graaf

Yale University School of Medicine, Department of Diagnostic Radiology, MR Research Center (MRRC), 300 Cedar Street, New Haven, CT 06520, USA

ARTICLE INFO

Article history:
Received 1 December 2009
Revised 9 March 2010
Available online 11 March 2010

Keywords:
Individual coil
Magnetic field modeling
Magnetic field gradients
Spherical harmonic functions

ABSTRACT

A set of generic, circular individual coils is shown to be capable of generating highly complex magnetic field distributions in a flexible fashion. Arbitrarily oriented linear field gradients can be generated in three-dimensional as well as sliced volumes at amplitudes that allow imaging applications. The multi-coil approach permits the simultaneous generation of linear MRI encoding fields and complex shim fields by the same setup, thereby reducing system complexity. The choice of the sensitive volume over which the magnetic fields are optimized remains temporally and spatially variable at all times. The restriction of the field synthesis to experimentally relevant, smaller volumes such as single slices directly translates into improved efficiency, i.e. higher magnetic field amplitudes and/or reduced coil currents. For applications like arterial spin labeling, signal spoiling and diffusion weighting, perfect linearity of the gradient fields is not required and reduced demands on accuracy can also be readily translated into improved efficiency. The first experimental realization was achieved for mouse head MRI with 24 coils that were mounted on the surface of a cylindrical former. Oblique linear field gradients of 20 kHz/cm (47 mT/m) were generated with a maximum current of 1.4 A which allowed radial imaging of a mouse head. The potential of the new approach for generating arbitrary magnetic field shapes is demonstrated by synthesizing the more complex, higher order spherical harmonic magnetic field distributions *X*2–*Y*2, *Z*2 and *Z*2*X*. The new multi-coil approach provides the framework for the integration of conventional imaging and shim coils into a single multi-coil system in which shape, strength, accuracy and spatial coverage of the magnetic field can be specifically optimized for the application at hand.

© 2010 Elsevier Inc. All rights reserved.

1. Introduction

Magnetic resonance (MR) imaging methods commonly use linear gradient fields to achieve spatial encoding of the nuclear spin system. The three gradient fields that are typically oriented along a Cartesian coordinate system *x*, *y* and *z* are among the most essential components of any MR imaging system, and since the early days of MR imaging [1] they are generated by specific coils, one for each field term. The design of the gradient coils aims at accurate field distributions at maximal strength, slew rate and efficiency. Although variable shape gradient systems have been presented for special applications [2,3], gradient systems are still typically constructed on a cylinder before they are fitted into the magnet bore to closely surround the object or patient and the RF coil(s). Design methods like the target field approach [4] and improvements of the gradient coil design such as the self-shielding of gradient coils [5] or the so-called 3D current geometry [6], replaced the early relatively simple Golay-type gradient systems [7–10] with highly advanced and much more complex gradient designs. Amongst others, state-of-the-art gradient systems have allowed the imaging of single cells [11], the mapping of orientation columns in human visual cortex [12] and the laminar specificity of functional MRI [13].

Conventional gradient/shim coils are of a fixed design, in which each coil produces a given magnetic field distribution over a given 'diameter spherical volume'. Here we show that a set of localized circular constant-current coils does provide the flexibility to design and produce linear and higher-order magnetic fields specifically tailored towards the subject and application at hand. The fundamental difference of this multi-coil approach and conventional gradients is that each coil contributes to every magnetic field. A regular grid of individual coils is shown to be capable of simultaneously generating linear and more complex gradient fields, e.g. for spatial MRI encoding and shimming, thereby offering a way to reduce the complexity of the applied coil system. The volume-of-interest (VOI) as well as the desired field accuracy do not need to be predefined with the multi-coil (MC) approach and, therefore, can be chosen and optimized on a subject- or even MR application-specific basis. Arbitrary magnetic fields can even be optimized and generated on a per-slice-basis, allowing efficiency gains relative to the synthesis of MC fields in larger volumes. Furthermore, reduced demands on accuracy can always be readily traded for improved

* Corresponding author. Address: MR Research Center (MRRC), 300 Cedar Street, TAC N142, New Haven, CT 06520, USA. Fax: +1 (203) 785 6643.
E-mail address: christoph.juchem@yale.edu (C. Juchem).

1090-7807/$ - see front matter © 2010 Elsevier Inc. All rights reserved.
doi:10.1016/j.jmr.2010.03.008

efficiency, i.e. higher magnetic field amplitudes and/or reduced coil currents.

We show that magnetic field gradients of high accuracy and high amplitude can be generated by a prototype MC setup and used to image the head of a mouse. To demonstrate the flexibility of the MC approach in generating arbitrarily shaped magnetic fields, we created and measured several higher order spherical harmonic (SH) field terms.

The study focuses on the introduction of the multi-coil concept and the characterization of its properties. No efficiency comparison of any kind with conventional state-of-the-art gradient systems has been done. All statements on efficiency in this study solely refer to different conditions of the multi-coil approach.

2. Methods

2.1. Theoretical generation of magnetic field gradients with a set of individual localized coils

The MR relevant z-component of the magnetic field generated by a circular, current driven loop in the center of the coordinate system with a coronal orientation, i.e. with a vector normal along the y-axis (posterior to anterior), can be derived analytically by integration of the Biot–Savart law to

$$B_z = \frac{\mu_0 \cdot I \cdot n}{2\pi} \frac{y}{\sqrt{(x^2+z^2)((r+\sqrt{x^2+z^2})^2+y^2)}} \times \left(-K(\kappa^2) + \frac{r^2+x^2+y^2+z^2}{(r-\sqrt{x^2+z^2})^2+y^2} E(\kappa^2)\right) \quad (1)$$

with μ_0 the magnetic field constant, I the constant current through the coil, n the number of turns, r the radius of the coil and x, y and z the Cartesian coordinates describing 3D space [14]. $K(\kappa^2)$ and $E(\kappa^2)$ refer to the complete elliptical integrals of the first and second kind, respectively, with $\kappa^2 = 4r(x^2+z^2)^{1/2}/[(r+(x^2+z^2)^{1/2})^2+y^2]$. Equivalent values in Hertz can be derived using the Larmor equation.

A total of 24 circular, constant-current coils (15 turns, center diameter 13 mm) were distributed in four rings of six coils each over a cylindrical surface with an outer diameter of 30 mm (Fig. 1). Given the total coil thickness of about 2 mm when wound from a 0.4 mm diameter wire, the distance of the coils to the isocenter of the magnet was 16 mm. The number of coils for the prototype realization in this study was determined by the number of available current supplies to drive them. The size and the positioning of the coils was chosen to closely surround the center part of the cylindrical volume.

Simulations have shown that for the selected coil diameter, bundle thickness and distances from the coil, the magnetic field of a real coil can be satisfactorily approximated by the field of a theoretical, single loop coil in which the current is scaled by the number of coil turns (data not shown). All field simulations presented in this study use that approximation.

Constrained least-squares fitting based on the Levenberg–Marquardt method was applied for magnetic field decomposition into the localized coil fields and the determination of the coil currents that were necessary to generate the different field shapes, either theoretically or experimentally. A centered, barrel-shaped volume that is large enough to cover the head of a mouse was chosen as VOI as well as single slices thereof. The VOI was derived from an elliptical volume with diameters of 16 mm along x and y, and 20 mm along z, which was further limited to 17 mm along z (VOI in Fig. 1). The color coding of the coils in Fig. 1 represents the current distribution that allows the creation of an example 10 kHz/cm X gradient inside the barrel-shaped 2.6 mL VOI for which the frequency distribution is color coded.

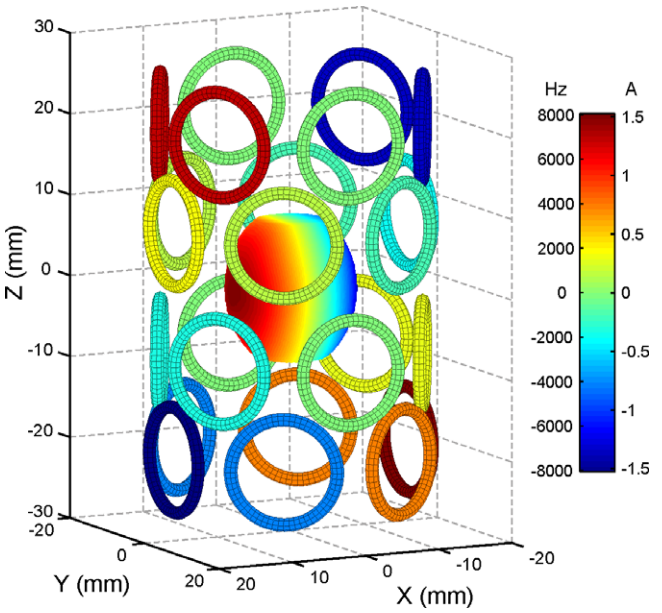

Fig. 1. Theoretical coil setup. A total of 24 coils (15 turns, diameter 13 mm) was arranged in four rows with six coils each on a cylindrical surface (diameter 30 mm). The coils' color coding represents the current distribution to create an example 10 kHz/cm X gradient in a centered, barrel-shaped VOI for which the frequency distribution is coded in color. See text for details.

The term efficiency refers to the amplitude of SH-shaped magnetic fields (in Hz/cm^n with n the SH order) that can be generated with the presented setup per unit current (in Ampere). The wire length per coil of 61 cm or the total wire length of the setup of about 15 m have not been considered.

2.2. General setup and field mapping

Experiments were performed on a 9.4 T magnet (Magnex Scientific, Oxford, UK) that was equipped with a Resonance Research (Resonance Research Inc., Billerica/MA, USA) gradient and shim system BFG-150/90-750-S interfaced to a Varian Direct Drive spectrometer and operated with VnmrJ 2.3A software (Varian Inc., Palo Alto/CA, USA). A home-built Bolinger RF coil [15] was used for RF transmission and signal reception. Multiple single-echo GE images (echo time 2.1/2.2/2.3/2.6/3.1/4.1/5.1 ms, repetition time 1.2 s, field-of-view $24 \times 24 \times 20$ mm^3, matrix $80 \times 80 \times 40$, bandwidth 417 kHz) were measured and phase maps were calculated using voxel-by-voxel temporal phase unwrapping. Field maps were computed using linear regression of signal phase and echo time [16].

2.3. Experimental realization of the individual localized coil setup

The coils were made of polyurethane/nylon coated copper magnet wire (Belden Electronic Division, St. Louis/MO, USA) of 0.4 mm diameter and mounted on the surface of an acrylic, cylindrical former with an outer diameter of 30 mm (Fig. 2A). The customized MC setup was placed firmly inside the RF resonater with no direct contact to the RF coil (Fig. 2B). The inner two rings of coils, i.e. 12 coils, were driven with a customized power supply in the ±1.0 A range. The outer two rings of coils were driven with a Bruker shim power supply in the ±1.9 A range. Home-written Matlab software (MathWorks, Natick/MA, USA) run on a PC or C software that was run on the console Linux computer allowed serial RS232 communication with the shim interface and application of the shim currents.

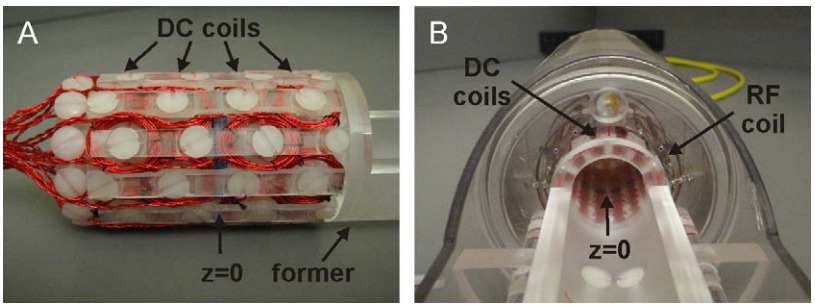

Fig. 2. Experimental realization of the multi-coil setup. (A) 24 individual coils (15 turns, diameter 13 mm) were placed on a cylindrical former made of acrylic tube. The inner diameter of the former of 25 mm allowed the placement of a glass bottle or a mouse cradle inside the device. (B) Firm mounting of the former inside the RF resonator provided a close integration of both systems and allowed their simultaneous use.

Each channel was calibrated based on nine independent field mapping experiments that covered the dynamic range of the corresponding current power supply. The shortest echo-time delay of 0.1 ms allowed the mapping of a frequency span up to 10 kHz, and longer delays were included to minimize the uncertainty of the voxel-specific frequency calculation. The latter proved to be particularly useful for the reduction of frequency noise in areas far away from the coils in which field changes as a result of coil current alterations were small. In combination with strong gradient fields close to the coils, however, long delays could lead to signal dropout and erroneous frequency values. To this end, the maximum echo-time delay that was used in the frequency calculation was determined in a voxel-specific manner based on an error threshold of the phase-delay regression analysis. Voxels from single echo time images were rejected for further analysis if the calculated field value was >2 kHz and at the same time the average error value of the linear regression exceeded 2%. Voxels were rejected completely in the subsequent calibration analysis, if the regression analysis of the field amplitude (in Hertz) and the calibration current (in percent of the dynamic range) revealed slopes >5 Hz/% with an average error >10%. Rejected voxel values, which accounted for less than 1% in each of the 24 calibration field maps, were interpolated from neighboring positions.

Similarly, the conventional gradient and shim system was calibrated to allow the comparison of the SH fields generated with the MC approach with SH shapes provided by the conventional gradient and shim system. The average error of the linear regression between the applied shim settings and the generated SH term was <0.5% in all cases.

2.4. Radial MR imaging with a set of individual localized coils

A slice-selective spin-echo experiment was extended by a projection encoding scheme consisting of 192 equiangular steps between 0 degrees and 180 degrees to allow radial imaging of a mouse head (Fig. 3A). A total of 160 complex data points were acquired over a 50 kHz spectral width in the presence of a 20 kHz/cm (or 47 mT/m) readout gradient to achieve a 25 mm projection length.

Similarly, radial imaging was done with the MC coil array at identical settings to prove its capacity of generating the necessary oblique gradient fields at the required accuracy and strength. Since not all of the MC current amplifiers were switchable in the prototype setup, the effect of the constant MC-generated gradient was canceled by conventional gradient fields as long as it was not needed, i.e. before the intended start of the readout period (Fig. 3B). The slice selection gradients as well as the readout preparation were also achieved with the scanners' built-in gradient set. Image reconstruction was achieved by inverse Radon transformation with spline interpolation and Shepp-Logan filtering.

2.5. Computational basis, algorithms and software

All image and field map processing, volume extraction, magnetic field simulations, field decomposition and modeling, coil calibrations and field analysis were done with customized Matlab software (MathWorks, Natick/MA, USA).

3. Results

3.1. Generation of magnetic field gradients with a set of individual localized coils

Theoretical, magnetic field gradients *X*, *Y*, *Z* and *XY* with 2 kHz/cm field amplitudes were modeled with the theoretical 24 coil setup for the barrel-shaped VOI (Table 1). The fitting was constrained by the maximum, experimentally available currents of 1.0 A and 1.9 A for the channels driven by the home-built and the Bruker power supply, respectively. Orthogonal sections through the obtained *XY* gradient field (Fig. 4, lower images) look virtually identical to the *XY* target field (Fig. 4, upper images). Similarly, no differences were visible between multi-coil and target *X*, *Y* or *Z* gradients (data not shown). In all cases, field distributions with $1 - R^2$ [17] values $<10^{-3}$ could be generated with the MC approach with an average deviation of <1% of the maximum field amplitude per term (Table 1). Maximum current amplitudes per channel of 220-306 mA were found. Notably, the maximum current is the current necessary to built a dedicated gradient setup if all coils were connected in series (with the number of coil turns downscaled according to the coils' current requirement). The sum over the 24 (magnitude) currents was 2.8–2.9 A. The current requirements for each coil stayed well below the constraints imposed by the limitations of the power supplies.

The decomposition into the calibrated basis fields led to sets of 24 currents which were then applied to generate the field terms experimentally. The quality of the field terms, therefore, could be analyzed at three different levels: theoretically, based on the predictions from the decomposition into the calibrated basis fields and from the experimental results. Table 2 summarizes the analysis of selected SH terms, among them a linear 2 kHz/cm *Y* gradient. Note that the experimental results are given as mean values with their standard deviations from at least six independent scans that originated from four different studies, i.e. experiment days. Experiments were extremely reproducible with standard deviations in the order of 0.2% or below.

3.2. Theoretical and experimental generation of a 2 kHz/cm XY gradient

The 2 kHz/cm *XY* gradient from Fig. 4 has been selected to provide an in-depth demonstration of typical MC characteristics, both,

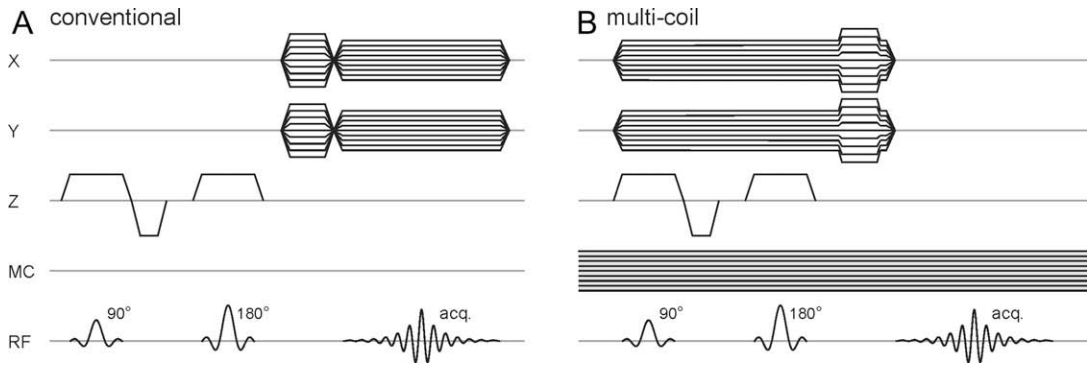

Fig. 3. Radial MR imaging with a set of individual coils. (A) A slice-specific spin-echo sequence was extended by a radial projection scheme to allow radial imaging of a mouse head. All gradients of the 'conventional' reference image were generated by the scanners' built-in gradient system. (B) Gradient fields as being generated with the MC coil array were used for radial projection readout in a similar MR sequence. The gradients other than the projection readout had to be provided by the scanners' gradient system, since not all of the MC power supplies were switchable yet. Note, that the MC gradient was permanently on, but was canceled with standard gradients as long as it was not needed.

Table 1
Theoretical generation of 2 kHz/cm *X*, *Y*, *Z* and *XY* gradient fields with the MC coil approach.

	X	*Y*	*Z*	*XY*
Maximum current (mA)	306	306	220	295
Current sum (mA)	2808	2808	2884	2906
Average difference (%)	0.36	0.36	0.89	0.36
$1 - R^2$ measure	0.00015	0.00015	0.00075	0.00015

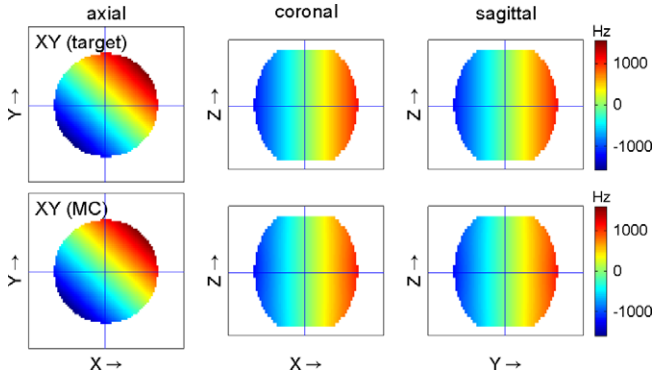

Fig. 4. Theoretical MC gradient generation in a 2.6 mL barrel-shaped volume with a set of 24 circular, individual coils. Orthogonal sections through a synthesized 2 kHz/cm *XY* gradient field (second row) look virtually identical to the target field shape (first row).

theoretically and in its experimental realization with a set of individual localized coils.

To this end, the target field distribution was decomposed into the 24 calibrated coil fields and the set of 24 coil currents was applied to experimentally generate the magnetic field distribution (Fig. 5A). The generated field resembled the target field distribution well with an $1 - R^2$ of 10^{-4} and an average deviation from the target field of 0.5% (Fig. 5A, second row). First order SH decomposition revealed *X*, *Y* and *Z* gradient contributions of 1404 Hz/cm, 1403 Hz/cm and −5 Hz/cm, respectively, with deviations from the nominal values of 1414 Hz/cm, 1414 Hz/cm and 0 Hz/cm below 1%. The maximum coil current was 330 mA and the limitations of the current power supplies had no effect for the selected 2 kHz/cm gradient amplitude, i.e. the fit was effectively unconstrained. For comparison, the residual field deviation between the target and the theoretical MC fields is shown in the third row of Fig. 5A. The similarity of the patterns in rows two and three of Fig. 5A demonstrates the fact that theoretically predicted and experimentally realized fields are in excellent agreement. Any deviations between target and experimental fields can thus be accurately predicted through theoretical calculations.

The coil currents that were necessary to generate a given magnetic field distribution were not only determined by the field amplitude, but they were also largely affected by the desired accuracy. To this end, the efficiency of the MC setup (in [Hz cm^{-1} A^{-1}]) could always be increased at the cost of a degradation of the achieved field accuracy. The introduction of a 250 mA current limit per coil allowed the synthesis of a still near-perfect *XY* gradient term, at a 23% improved efficiency (Fig. 5B). The generated field

Table 2
Analysis of field characteristics for the *Y* (2 kHz/cm), *X2–Y2* (1 kHz/cm^2), *Z2* (1 kHz/cm^2) and *Z2X* (1 kHz/cm^3) magnetic field terms in a barrel-shaped volume based on the theoretical synthesis of MC fields, the prediction of the experimental results from the decomposition of the target fields into the 24 calibrated MC basis fields and the experimental realization of the MC field synthesis. Quality measures for experimentally acquired magnetic fields are given as mean values and standard deviations of 6 independent scans from four different studies.

Field shape	Theoretical multi-coil fields				Calibrated multi-coil fields			
	Y	*X2-Y2*	*Z2*	*Z2X*	*Y*	*X2-Y2*	*Z2*	*Z2X*
Average difference (%)	0.36	0.72	2.05	1.24	0.39	0.95	1.78	1.20
$1 - R^2$ measure	0.00015	0.00105	0.00679	0.00730	0.00013	0.00139	0.00470	0.00577
Amplitude (Hz/cm^n)	1999.7	998.9	992.9	992.0	1999.7	998.6	995.1	993.7

	Experimental multi-coil fields			
	Y	*X2–Y2*	*Z2*	*Z2X*
Average difference (%)	0.47 ± 0.08	1.65 ± 0.30	1.89 ± 0.04	1.29 ± 0.05
$1 - R^2$ measure	0.00785 ± 0.00286	0.00785 ± 0.00286	0.00564 ± 0.00018	0.01084 ± 0.00029
Amplitude (Hz/cm^n)	1998.4 ± 1.3	1002.3 ± 1.7	981.1 ± 1.0	989.3 ± 1.9

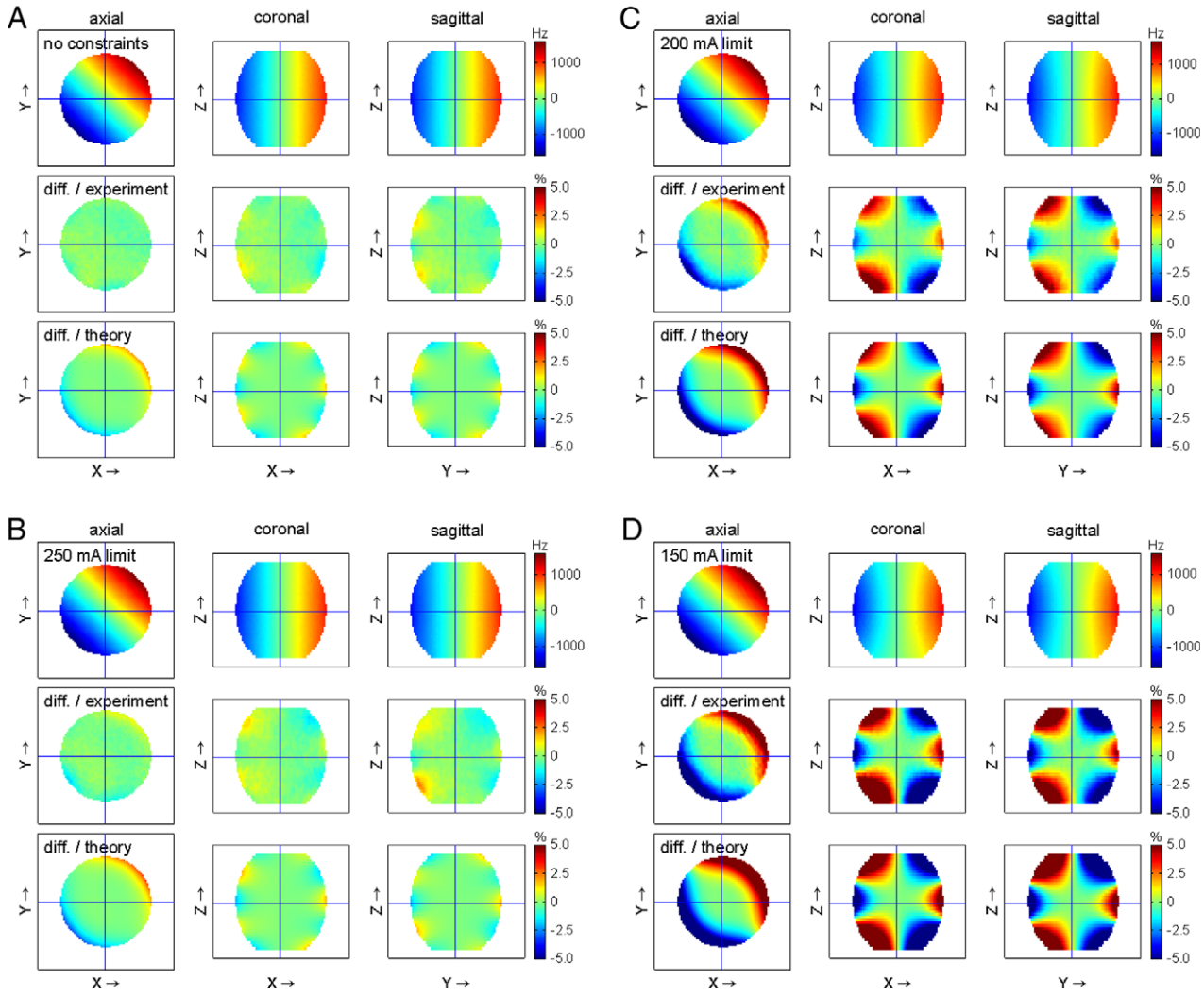

Fig. 5. Experimental MC gradient generation of a 2 kHz/cm *XY* gradient field in a 2.6 mL barrel-shaped volume. (A) An unconstrained MC analysis led to a maximum coil current of 330 mA, the generated field resembled the target field distribution well (first row) and deviations from it were small (second row). (B) A 23% efficiency improvement could be achieved at minimum cost by constraining the maximum coil current to 250 mA. (C) The field accuracy at a further limitation of the maximum coil currents to 200 mA corresponding to a 38% efficiency increase might still be acceptable, while (D) considerable field degradations were observed at a 54% lowered maximum current of 150 mA. See text for details.

had an $1 - R^2$ value of 10^{-3} with an average deviation from the target *XY* gradient field of 1.0% (first/second row, Table 2). SH decomposition revealed linear terms *X*, *Y* and *Z* of 1399 Hz/cm, 1399 Hz/cm and −5 Hz/cm, respectively.

The field decomposition into MC fields with 200 mA current constraints led to a 38% efficiency increase, however, the inaccuracies of the generated *XY* gradient term became more apparent (Fig. 5C). Achieved gradient amplitudes along *X* and *Y* of 1381 Hz/cm and 1386 Hz/cm, respectively, were somewhat reduced with a *Z* component of −6 Hz/cm. An $1 - R^2$ value of 0.003 and an average deviation from the *XY* target field of 2.0%, however, might be acceptable or not, based on the application of such field gradient. Again, the decomposition of the target field into theoretical coil fields closely matched the experimental outcome (Fig. 5C, bottom row).

Although the efficiency improvement of 54% was highest with a current constraint of 150 mA, the generated magnetic field only poorly resembled the target field distribution (Fig. 5D). While the gradient contributions of 1364 Hz/cm for the *X*, 1372 Hz/cm for the *Y* and −6 Hz/cm for the *Z* gradient were still close to target field amplitudes, the generated field is characterized by the presence of higher-order imperfections which is expressed by the $1 - R^2$ value of 0.01 and an averaged deviation of 3.4%.

For comparison, a 2 kHz/cm *XY* gradient field as generated by the scanners' built-in gradient system was analyzed. The quality assessment revealed an $1 - R^2$ value of 10^{-4} over the considered, barrel-shaped VOI for (*X*, *Y* or) *XY* gradients with an average deviation from the target field of less than 1%, thereby proving the high quality of the available gradient system. The *X*, *Y* and *Z* contributions to the generated field were 1404 Hz/cm, 1401 Hz/cm and −5 Hz/cm, respectively.

Further efficiency and accuracy improvements were achieved with the MC approach by VOI reduction from the barrel-shaped volume to slices, i.e. subvolumes, thereof. Similarly to the analysis of the barrel-shaped VOI in Fig. 5, the results of a slice-specific MC field generation analysis are summarized in Fig. 6 for a center 0.5 mm thick slice (0.10 mL or 2244 voxel) with an offset of −0.25 mm and a peripheral 0.5 mm thick slice (0.03 mL or 692 voxel) with an offset of −9.75 mm.

Field decomposition of the center slice without current limitation and with current constraints of 250 mA, 200 mA and 150 mA led to $1 - R^2$ values of $<10^{-4}$, 10^{-4}, 2×10^{-4} and 5×10^{-4} with

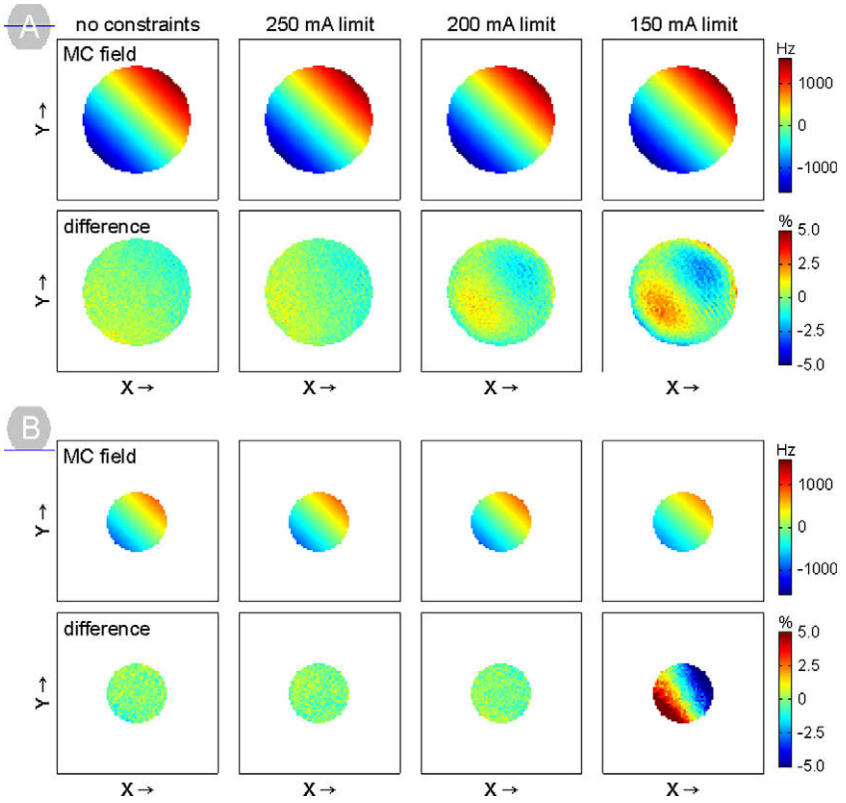

Fig. 6. Experimental MC gradient generation of a 2 kHz/cm *XY* gradient field in sliced subvolumes of the barrel-shaped basic volume. (A) Improved field accuracy was achieved in a central slice (A: offset -0.25 mm, volume 0.10 mL) as well as in a peripheral slice (B: offset -9.25 mm, volume 0.03 mL) for all current constraints when compared to the consideration of the whole barrel-shaped VOI (Fig. 5). For unchanged accuracy, these improvements could be directly transferred to strongly reduced maximal coil currents and improved gradient efficiencies.

average deviations from the *XY* target field gradient of 0.4%, 0.5%, 0.6% and 1.0%, respectively (Fig. 6A, first row). The corresponding gradient components were 1403 Hz/cm, 1397 Hz/cm, 1399 Hz/cm and 1397 Hz/cm along *x* and 1404 Hz/cm, 1408 Hz/cm, 1408 Hz/cm and 1405 Hz/cm along *y*. The synthesized field closely resembled the target *XY* field even for a reduction of the maximum current of the unconstrained fit of 381 mA by 71% to 150 mA, i.e. the efficiency of the field generation was increased by 65%. Deviations worsened gradually as shown in the difference maps (second row) and might be acceptable or not depending on the MR application of the gradient.

The *X* and *Y* terms that were generated in the same centered slice by the scanner's built-in gradient system were 1404 Hz/cm and 1402 Hz/cm, respectively, revealing an $1 - R^2$ of 10^{-4} and an average deviation from the target *XY* gradient of 0.4%.

For the peripheral slice, the synthesized *XY* gradient had $1 - R^2$ values of 3×10^{-4}, 3×10^{-4}, 3×10^{-4} and 0.02 and average deviations from the *XY* target field of 0.7%, 0.7%, 0.7% and 6.1% for the current constraints ranging from an open fit down to 150 mA (Fig. 6B, first row). The *X* gradient component was measured to 1416 Hz/cm, 1409 Hz/cm, 1403 Hz/cm and 1280 Hz/cm and the generated *Y* gradient component was 1422 Hz/cm, 1418 Hz/cm, 1409 Hz/cm and 1281 Hz/cm. Compared to the center slice, the residual deviations from the target field shape remained below the noise level for efficiency improvements of 16% and 32%, but worsened strongly for a current restriction of 150 mA. For the peripheral slice considered here, an efficiency improvement of 32% is certainly possible, but further current limitations cannot be accepted in MR applications.

For comparison, the application of a 2 kHz/cm *XY* gradient with the scanner's built-in gradient system in the peripheral slice led to an 1408 Hz/cm *X* term and an 1408 Hz/cm *Y* term. The $1 - R^2$ was 2×10^{-4} and the average deviation from the target field was 0.7%.

3.3. Radial MR imaging with a set of individual localized coils

Magnetic field gradients as generated with the MC approach allowed radial imaging of a mouse head (Fig. 7A). For comparison, Fig. 7B shows the equivalent image acquired with the conventional scanners' gradient system only. Beside some differences in image contrast, no major differences in signal strength are visible. All minor image artifacts could be attributed to the inherent characteristics of acquiring and processing radial imaging data, i.e. none of the visible artifacts were related to the MC readout fields.

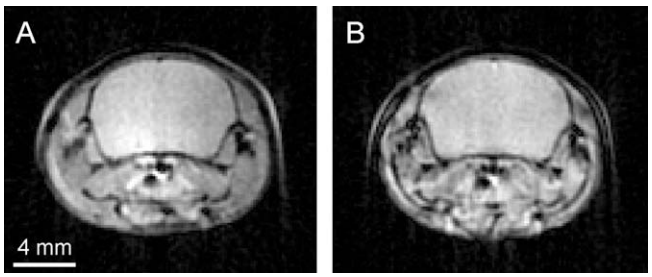

Fig. 7. Radial MR imaging with MC-generated gradient fields. (A) The synthesis of gradient fields at 192 rotation angles with the MC approach enabled radial imaging with the MR sequence described in Fig. 3B. The MC image looks identical to the one acquired with a conventional gradient system only (B) and no method specific artifacts were observed.

3.4. Generation of complex magnetic field shapes

The MC method is not limited to the synthesis of relatively simple, linear gradient fields. Second and third order SH terms were modeled to demonstrate the ability of the MC approach to generate more complex field distributions (Fig. 8).

The unconstrained fit of a 1 kHz/cm^2 *X*2–*Y*2 term over the full, barrel-shaped VOI into the MC fields led to a maximum current of 980 mA and a current sum of 8.7 A. The generated, experimental field term closely resembles the target field with an $1 - R^2$ of 0.008, an averaged deviation of 1.6% and a *X*2–*Y*2 amplitude of 1002 Hz/cm^2 (Table 2).

Similarly, a 1 kHz/cm^2 *Z*2 term was generated with a 434 mA maximum current, corresponding to 22.5% of the dynamic range, a 6.0 A current sum, an $1 - R^2$ value of 0.006 and an average deviation of 1.9%. The amplitude of the experimentally generated *Z*2 term was 981 Hz/cm^2 (Table 2).

The third order SH term *Z*2*X* was synthesized at 1 kHz/cm^3 by a 783 mA maximum current, a current sum of 6.0 A, and an $1 - R^2$ value of 0.01 (Fig. 8). The *Z*2*X* amplitude of the created field was 989 Hz/cm^3 with an averaged deviation from the *Z*2*X* target field of 1.3% (Table 2). Note that the 1.1% (11 Hz/cm^3) deviation of the experimental *Z*2*X* amplitude could be predicted based on the theoretical and the calibrated coil fields. It can be easily rescaled to match the target amplitude at a minor 0.01% degradation of the average deviation quality measure.

For comparison, the same SH terms *X*2-*Y*2, *Z*2 and *Z*2*X* were generated with the scanners' built-in shim system at 400 Hz/cm^2, 1 kHz/cm^2 and 25 Hz/cm^3, respectively. Note that the *X*2-*Y*2 and the *Z*2*X* amplitudes had to be lowered to meet the available amplitude range of the used shim system. The measured amplitudes of 398 Hz/cm^2, 1006 Hz/cm^2 and 25.1 Hz/cm^3 for the *X*2–*Y*2, *Z*2 and *Z*2*X* terms closely matched the target field strengths and, thereby, proved the quality of the field calibration. Average deviations of 6.0%, 2.2% and 60.7% as well as $1 - R^2$ values of 0.042, 0.006 and 0.993, respectively, showed that the *X*2–*Y*2 term and even more so the *Z*2*X* term contained large field impurities. The artificial contributions in the *X*2-*Y*2 were mostly linear, however, the impurities of the *Z*2*X* term consisted of a complex combination of a multitude of different order SH terms and, correspondingly, the computational removal of the linear terms from the measured *Z*2*X* field reduced the $1 - R^2$ value to 0.146 and the average deviation to 7.5% only.

For the *Z*2 term being generated with the MC approach, the limitation of the full barrel-shaped VOI to the centered slice that was used for the slice-specific analysis in Fig. 6A led to a reduction of the maximal current requirement for the unconstrained condition from 434 mA to 99 mA, corresponding to an efficiency improvement of 338% from 2.3 kHz cm^{-2} A^{-1} to 10.1 kHz cm^{-2} A^{-1} (data not shown). The integral current requirement was reduced from 6.0 A to 0.8 A. Notably, at the same time the $1 - R^2$ and the average error could be lowered to $<10^{-3}$ and 0.9%, respectively, i.e. the accuracy of the generated field term was also improved. At this point, the gain in efficiency already allowed the generation of a 5 kHz/cm^2 *Z*2 term with less than 50% of the dynamic range of the used MC current amplifiers. For the same 5 kHz/cm^2 *Z*2 field shape, limiting the maximum current to 200 mA led to an $1 - R^2$ of < 10–3 and an average error of 0.9%, and an $1 - R^2$ value of 0.001 and an average error of 1.8% were achieved with a 150 mA current constraint. The accuracy of the latter field distribution is comparable to the *Z*2 field term that was synthesized based on an open fit of the full barrel-shaped VOI, but the efficiency of the latter was with 33.3 kHz cm^{-2} A^{-1} more than 14 times higher.

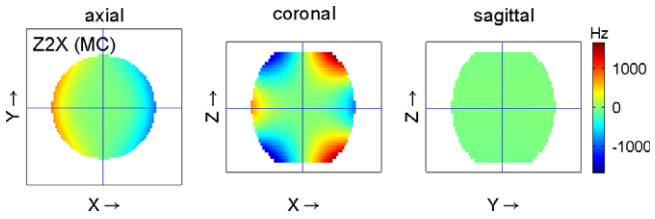

Fig. 8. The ability of the MC approach to synthesize complex field distributions is demonstrated by the generation of a third order *Z*2*X* term at 1 kHz/cm^3. The experimentally measured term resembled the target field distribution with a high degree of similarity. See text for details.

4. Discussion

It has been shown that magnetic gradient and shim fields generated with a set of individual, localized coils provide a flexible alternative to the use of dedicated gradient and shim coils. The new multi-coil approach is capable of synthesizing a multitude of magnetic field shapes with high accuracy and amplitude in volumes that are commonly used in small-bore MR scanners. The experiment-specific VOI selection enabled the MC approach to maximize the efficiency and/or the accuracy of the gradient field generation in a direct and very flexible manner.

Localized, constant-current coils have been used before in MR applications to generate local field gradients [18–20]. In these applications, however, the particular shape of a few coils was essential and only simple field distributions were created. Furthermore, modular [21] and composite [22] gradient coils have been presented for improved performance and reduced nerve stimulation. These coils, like conventional gradient coils, are designed to provide one single field term per coil. Here, the resultant field distribution is no longer predominantly determined by the shape of a coil and the field it generates, but by the number of basis fields and the size of the concomitant parameter space. The presented MC approach can be understood as a generalization and 3D extension of the MAMBA method [23,24]. In principle, the complexity of 3D fields that can be generated with the MC approach is only limited by the number of coils. Simulations have shown that all first-to-fourth order SH terms can be generated with a similar setup of 100 coils [25] and even the presented miniaturized MC setup consisting of 24 coils was already able to generate a variety of SH terms. Potential applications might include the generation of non-linear field shapes for spatial localization with advanced imaging techniques [26]. Imaging algorithms will no longer have to chose from a limited set of available field shapes. The MC approach will allow, within reasonable limits, the generation of field shapes that are most advantageous for such imaging techniques. Furthermore, the quality of active field homogenization (i.e. 'shimming') is expected to strongly benefit from the new MC approach through its ability to synthesize advanced shim field distributions. This will be particularly relevant for areas of localized and high amplitude field distortions as are found in the human prefrontal cortex or in rodent brain close to the auditory cavities. The multitude of high amplitude, local basis fields of the MC approach is inherently better suited to correct focal field distortions than the low amplitude and shallow SH shim fields currently available. A highly symmetric MC array was placed on a cylindrical surface in this study for the first realization of the MC concept. Simulations of MC shimming of the human brain have shown, however, that the method by no means relies on symmetric coil positioning or a cylindrical base geometry [27].

Quantitative B_1 field mapping with the prototype MC setup inside the RF resonater revealed a largely homogenous damping by a factor of two when compared to the RF resonater alone. The highest sensitivity of the RF circuitry was not essential for the proof of

principle of the MC method presented here, but losses are not acceptable for most applications. Future improvements include a closer integration of the RF coil and the multi-coil system similar to the body RF coil and the gradient system in whole body human MR systems, or the reversion of the setup geometry and the placement of the RF resonator inside the multi-coil setup.

The MC approach relies on a high degree of positioning reproducibility in order to allow high quality field syntheses especially if small volumes such as single slices are considered. Solid mounting of the coils on the surface of an acrylic former and a screw-based fixation of the former inside the RF probe and the magnet bore ensured the reproducibility of the coil positioning even if the MR probe and the MC setup were taken apart multiple times. Since the MC approach does not critically rely on the shape of a single coil field and the VOI position relative to it, reproducible offsets of several millimeters or rotations between the MC setup and the VOI can be accommodated by an altered MC current distribution.

High quality field mapping was an essential prerequisite in this study. Geometric image distortions were negligible due to the large imaging bandwidth of more than 400 kHz and an extended series of short- to long-echo delays assured reliable phase unwrapping while minimizing the frequency noise of the field maps. The results shown here are representative results and are reproducibly achieved with the presented setup. All experimental results were obtained weeks to months following the MC calibration, thereby demonstrating the stability of the MC setup and calibration. The physical field errors that were caused by positioning inaccuracies of the presented MC prototype inside the magnet were always as small as the residual low order field gradient that is shown in the axial view of the second row of Fig. 5A. Even more rigorous and more permanent mounting (e.g. by embedding in epoxy) of the next generation MC setup is expected to further reduce these positional errors. Notably, the magnetic field shapes were directly decomposed into the MC basis set, i.e. the gradient amplitudes themselves were not part of the cost function. The residual amplitude imperfections (which were in the order of 1% or below) are well-understood and can be easily eliminated by rescaling the coil currents. Larger field inaccuracies that were due to current or shape limitations of the presented 24 MC setup for high amplitude or complex fields, were well-predictable, both theoretically and experimentally. This is relevant for making the best decision in terms of accuracy versus efficiency, and it allows for post-processing corrections of images acquired with imperfect, but reproducible fields [28]. The established framework provides a solid basis for future MC developments with an increased number of coils, the modification of the coil characteristics such as position, diameter, shape or the extension of the MC setup to human applications.

Gradient fields were generated at an efficiency of 14 kHz cm^{-1} A^{-1} in this study and provided a 20 kHz/cm (or 47 mT/m) readout gradient at 1.4 A maximum current. For a fair comparison of the efficiencies of the MC approach with traditional gradient and shim systems, the dimensions of the setups had to be taken into account as well as the number of turns or, equivalently, the length of the wire that was used for winding the coils. Unfortunately, such details of state-of-the-art gradient and shim coils are not easily accessible. However, a comprehensive and quantitative comparison of the efficiencies of the MC approach with state-of-the-art gradient systems was not intended here. The presented MC approach does not aim at competing with a well-designed, conventional gradient coil. In reality, it is likely that the efficiency over a large and static VOI is near-optimal when created with a conventional state-of-the-art gradient system. However, a prominent advantage of the new approach is its ability to flexibly account for the experimental conditions. The efficiency for the generation of the relatively simple *XY* gradient could be improved multifold in this study by limiting the VOI to single slices. For more complex field shapes like the *Z2* term, efficiency improvements of more than an order of magnitude were achieved without compromising the quality of the resultant field shape. Remember that efficiency comparisons in this study solely address different conditions of the MC approach and do not refer to conventional gradient systems. Notably, field variations outside the target volume were relatively smooth in the considered cases and ambiguous field conditions or folding back of signal was never observed.

Although sufficient to perform radial MRI of the mouse head, the gradient amplitudes that were generated with the current MC setup were not yet at the level of those of a conventional gradient system. Further increases of the available gradient amplitude without penalty on the field accuracy may be achieved by an increase of the applicable current range, the extension of the number of coil turns or even more miniaturized gaps between the coils and the VOI. However, these approaches will face the obvious obstacles of limited ampacity of the coil wire, the need for water cooling at increased power deposition, and limited space on the surface as well as on the inside of the coil former.

The MC generated field shapes were compared in this study to magnetic field distributions that were provided by the scanners' built-in gradient and shim system. For the MC approach, the *X*, *Y* and *Z* gradient components were determined by the calibration of the particular coils as well as their interplay to synthesize the designated field term. For the scanners' built-in gradient system, however, the accuracy of the achieved gradient amplitudes mostly reflects the accuracy of the gradient calibration. In the same vein, besides the excellent performance of the scanners' gradient system, considerable imperfections of the *X2-Y2* and the *Z2X* term were determined for the shim system. In practice, these imperfections are not necessarily a problem, if they can be resembled by other supported shim terms and if shim-to-shim interactions are taken into account in the shimming process. To this end, the comparison of the MC approach to the hardware of our specific system aimed solely at providing the reader a feel for the field properties described in this paper and must not be overinterpreted, since conditions were not always the same.

Heat generation has not been a problem with the presented MC setup and a current range of 1-2 A. Even during continuous usage of the MC array for radial imaging, i.e. at 100% duty cycle, no cooling was necessary. The small current range also minimized Lorentz forces, and therefore the physical stress onto the wire mounting and the creation of acoustic noise. The inductance of the MC coils is only 10 μH which will facilitate their switching with a low voltage amplifier. Inductive coupling between the coils might become a problem when coil currents are altered e.g. to generate full scale MR imaging and spectroscopy sequences in future applications. First experiments at switching times of 25 μs have shown, however, that induced voltages do not exceed 0.1% of the switching amplitude. The distance of the MC setup to the conductive structures of the magnet most likely prevents the generation of eddy currents. If this assumption holds true, preemphasis, as is used for dynamic shim updating via standard SH shim coils [29], will not be necessary and complex field shapes can be applied at the same short timescale.

The MC approach does not only enable the flexible generation of advanced gradient/shim fields, but it will also allow the explicit, subject- and application-specific consideration of secondary characteristics of MR experiments such as the creation of noise, heat, or mechanical stress. Furthermore, imposed current limitations or partial usage of the MC system provide handles on the total and local power deposition. The problem of peripheral nerve stimulation can be addressed by appropriate field design.

The installation and operation of the MC setup required various non-standard hardware, software and methods. A close integration of the MC array, the RF coil and the animal/subject positioning was

necessary to assure the highest sensitivity for both the MC and the RF systems. A series of current supplies equaling the number of coils had to be available and methods had to exist to drive them. Routines and analysis methods had to be provided for the calibration of the MC fields as well as the fitting algorithms for the decomposition of VOI-specific target fields into the MC basis set. However, even though advanced software and computational methods were needed to run the MC experiments presented in this study, the procedures can be easily automated and made accessible for the routine user. This does not only refer to the full calibration of the MC system, but also to the predefinition of field shapes, amplitudes and sensitive volumes to be used in MR applications.

A new MC approach has been presented that provides the framework for the integration of conventional spatial encoding and field correction coils into a novel and powerful field modeling system.

Acknowledgments

This research was supported by a Brown–Coxe Fellowship and NIH Grants R21/R33-CA118503, R01-EB000473 and P30-NS052519.

References

[1] P.C. Lauterbur, Image formation by induced local interactions: examples employing nuclear magnetic resonance, Nature 242 (1973) 190–191.
[2] A. Jasinski, P. Kozlowski, A. Urbanski, J.K. Saunders, Hexagonal surface gradient coil for localized MRS of the heart, Magn. Reson. Med. 21 (1991) 296–301.
[3] S.J. Dodd, C. Ho, Short planar gradient coils for MR microscopy using concentric return paths, J. Magn. Reson. 156 (2002) 1–9.
[4] R. Turner, A target field approach to optimal coil design, J. Phys. D: Appl. Phys. 19 (1986) 147–151.
[5] P.B. Roemer, J.S. Hickley, Self-shielded Gradient Coils for Nuclear Magnetic Resonance Imaging, US Patent 4737,716, 1988.
[6] S. Shvartsman, M. Morich, G. Demeester, Z. Zhai, Ultrashort shielded gradient coil design with 3D geometry, Concepts Magn. Reson. 26B (2005) 1–15.
[7] F. Romeo, D.I. Hoult, Magnet field profiling: analysis and correcting coil design, Magn. Reson. Med. 1 (1984) 44–65.
[8] M.J.E. Golay, Magnetic Field Control Apparatus, US patent 3515,979, 1970.
[9] R. Bowtell, P. Mansfield, Gradient coil design using active magnetic screening, Magn. Reson. Med. 17 (1991) 15–19 (discussion 19–21).
[10] R. Turner, Gradient coil design: a review of methods, Magn. Reson. Imaging 11 (1993) 903–920.
[11] N.R. Aiken, E.W. Hsu, S.J. Blackband, A review of NMR microimaging studies of single cells, J. Magn. Reson. Anal. 1 (1995) 41.
[12] E. Yacoub, N. Harel, K. Ugurbil, High-field fMRI unveils orientation columns in humans, Proc. Natl. Acad. Sci. U. S. A. 105 (2008) 10607–10612.
[13] A.C. Silva, A.P. Koretsky, Laminar specificity of functional MRI onset times during somatosensory stimulation in rat, Proc. Natl. Acad. Sci. U. S. A. 99 (2002) 15182–15187.
[14] R.A. Schill, General relation for the vector magnetic field of a circular current loop: a closer look, IEEE Trans. Magn. 39 (2003) 961–967.
[15] L. Bolinger, M.G. Prammer, J.S.J. Leigh, A multiple-frequency coil with a highly uniform B1 field, J. Magn. Reson. 81 (1988) 162–166.
[16] R.A. de Graaf, In vivo NMR Spectroscopy: Principles and Techniques, John Wiley and Sons, London, 2008. pp. 216–218.
[17] C. Juchem, B. Muller-Bierl, F. Schick, N.K. Logothetis, J. Pfeuffer, Combined passive and active shimming for in vivo MR spectroscopy at high magnetic fields, J. Magn. Reson. 183 (2006) 278–289.
[18] J.J. Hsu, G.H. Glover, Mitigation of susceptibility-induced signal loss in neuroimaging using localized shim coils, Magn. Reson. Med. 53 (2005) 243–248.
[19] B. Gleich, J. Weizenecker, Tomographic imaging using the nonlinear response of magnetic particles, Nature 435 (2005) 1214–1217.
[20] C. Juchem, T.W. Nixon, S. McIntyre, D.L. Rothman, R.A. de Graaf, Magnetic field homogenization of the human prefrontal cortex with a set of localized electrical coils, Magn. Reson. Med. 63 (2010) 171–180.
[21] P.R. Harvey, E. Katznelson, Modular gradient coil: a new concept in high-performance whole-body gradient coil design, Magn. Reson. Med. 42 (1999) 561–570.
[22] D.L. Parker, K.C. Goodrich, J.R. Hadley, S.-E. Kim, Sung M. Moon, B.A. Chronik, U. Fontius, F. Schmitt, Novel gradient coils designed using a boundary element method, Concepts Magn. Reson. 35B (2009) 89–97.
[23] K.J. Lee, M.N. Paley, I.D. Wilkinson, P.D. Griffiths, Fast two-dimensional MR imaging by multiple acquisition with micro B(0) array (MAMBA), Magn. Reson. Imaging 20 (2002) 119–125.
[24] K.J. Lee, M.N.J. Paley, D.C. Barber, I.D. Wilkinson, P.D. Griffiths, Target field design for MAMBA step fields, Concepts Magn. Reson. 20B (2004) 1–8.
[25] C. Juchem, D.L. Rothman, R.A. de Graaf, First-to-fourth Order Spherical Harmonics Shimming with a Grid of Circular Electrical Coils, ISMRM, Annual Meeting, Honolulu, HI/USA, 2009, pp. 3081.
[26] J. Hennig, A.M. Welz, G. Schultz, J. Korvink, Z. Liu, O. Speck, M. Zaitsev, Parallel imaging in non-bijective, curvilinear magnetic field gradients: a concept study, Magma 21 (2008) 5–14.
[27] C. Juchem, T.W. Nixon, M. Abildgaard, S. McIntyre, D.L. Rothman, R.A. de Graaf, Whole Brain Field Homogenization with Localized Electrical Coils, ISMRM, Annual Meeting, Honolulu, HI/USA, 2009, pp. 3079.
[28] P. Jezzard, R.S. Balaban, Correction for geometric distortion in echo planar images from B0 field variations, Magn. Reson. Med. 34 (1995) 65–73.
[29] K.M. Koch, S. McIntyre, T.W. Nixon, D.L. Rothman, R.A. de Graaf, Dynamic shim updating on the human brain, J. Magn. Reson. 180 (2006) 286–296.